RSC Advances

PAPER

View Article Online
View Journal | View Issue

Cite this: *RSC Adv.*, 2017, **7**, 18108

Structure and performance of a V_2O_5–WO_3/TiO_2–SiO_2 catalyst derived from blast furnace slag (BFS) for $DeNO_x$†

Tuyet-Suong Tran,[ab] Jian Yu,*[a] Changming Li,[a] Feng Guo,[a] Yusheng Zhang[a] and Guangwen Xu*[a]

The titanium-bearing blast furnace slag (BFS), a solid waste with high TiO_2 content (around 20%) and huge production (3.6 million tons per year), has caused serious environmental problems in China. The reuse of BFS in making $DeNO_x$ catalysts has been confirmed to be promising because of its low cost and high effectiveness for $DeNO_x$. In this work, four V_2O_5–WO_3/TiO_2–SiO_2 samples from BFS and commercial Ti/Si were made with different amounts of $Al_2O_3/Fe_2O_3/SO_4^{2-}$ dopants to reveal the unique structure effect of a slag-based catalyst on the catalytic behavior for $DeNO_x$. Catalyst characterization clarified that the $Al_2O_3/Fe_2O_3/SO_4^{2-}$ dopants from BFS may facilitate the formation of Ti–O–Si linkages with abundant structure defects. The structure possibly played a key role in acquiring a high surface area, well-dispersed active VO_x species, sufficient weak acid sites and a high amount of O_{ads} and V^{4+} species for the slag-based catalyst. These advantages in structure were confirmed by catalytic tests showing superior $DeNO_x$ performances. Nonetheless, too many SO_4^{2-} dopants caused agglomeration of TiO_2–SiO_2 particles, formation of strong acid sites and a high amount of O_{ads} species to negatively impact the $DeNO_x$ activity, selectivity and catalyst lifetime.

Received 29th January 2017
Accepted 15th March 2017

DOI: 10.1039/c7ra01252g

rsc.li/rsc-advances

1. Introduction

The vanadium-based catalysts, especially V_2O_5/TiO_2 doped with WO_3 or MoO_3, have achieved great success in selective catalytic reduction (SCR) of NO with NH_3 for their high activity and durability to SO_x poisoning.[1–14] Nevertheless, this kind of catalyst has a relatively high price, which restricts their wide use in combustion facilities of small to middle scale. On the other hand, the blast furnace slag (BFS), which contains about 20 wt% TiO_2, is a massive solid waste from the iron-steel industry. In China, it amounts 3.6 million tons per year, and would cause serious environmental problems without efficient treatment and reuse.[15,16] Considering the reuse of BFS as a Ti source, we have for the first time proposed the production of V–W–Ti catalysts for flue gas denitration ($DeNO_x$) from the slag. The idea was confirmed to be effective to lower the cost of SCR catalysts and simultaneously provides a new pathway to fully utilize BFS.[17]

Recent studies have shown that incorporation of some metal oxides such as Al_2O_3, SiO_2, Fe_2O_3 and CeO_2 into TiO_2 support as mechanical promoters enhanced $DeNO_x$ catalytic performance of the resulting catalysts because the promoters likely improve the dispersion and thermal stability of catalytic components.[3–7,18–23] Especially, TiO_2–SiO_2 has drawn particular attention because of its induced high $DeNO_x$ activity and low SO_2 oxidation activity. The structural advantages from doping SiO_2 are its enhanced dispersion and stabilization effects on anatase TiO_2 and VO_x species, together with the formation of more Brønsted acid sites needed for NO reduction.[5–7,19] As a matter of fact, the TiO_2–SiO_2 support with different TiO_2/SiO_2 ratios can be easily prepared in one step from BFS as shown by our recent work.[24] Besides providing low preparation cost as compared to methods based sol–gel or co-precipitation using pure chemicals, a distinguishing feature is its enabled high specific surface (427 $m^2\ g^{-1}$) and better $DeNO_x$ performance in a wide temperature window of 250–400 °C for the prepared catalyst. However, the TiO_2–SiO_2 support made from BFS has to contain some unavoidable dopant oxides such as Al_2O_3 and Fe_2O_3 to challenge the understanding of relationship between structure and function of the BFS-derived $DeNO_x$ catalysts. It is thus necessary to deeply get insight into the structure of the BFS-derived catalysts for achieving their better applications.

The present work aims at revealing the structure effect of BFS-derived catalysts on their superior catalytic performance for $DeNO_x$ by SCR. Two catalysts on TiO_2–SiO_2 support but with different amounts of $Al_2O_3/Fe_2O_3/SO_4^{2-}$ dopants were prepared from BFS by controls of H_2SO_4 concentration and pH value in

[a]State Key Laboratory of Multi-phase Complex Systems, Institute of Process Engineering, Chinese Academy of Sciences, Beijing 100190, China. E-mail: yujian@ipe.ac.cn; gwxu@ipe.ac.cn; Tel: +86-10-82629912

[b]University of Chinese Academy of Sciences, Beijing 100049, China

† Electronic supplementary information (ESI) available. See DOI: 10.1039/c7ra01252g

precipitation. The other two samples for comparison were prepared by traditional co-precipitation or sol–gel method using commercial inorganic or organic Ti/Si chemicals.[25,26] The SiO_2 content of all samples was nearly the same (about 0–10 wt%) as that in commercial SCR catalysts.[5,27] The structure of catalysts was obtained through characterizations using XRD, TG, BET, XPS, TPR, SEM, TEM and FT-IR for both fresh and spent catalysts, and the relationship between structure and dopants was clarified through correlating catalytic performance for SCR of NO by NH_3 and catalyst structure. This is further expected to deeply understand the mechanism of BFS-based $DeNO_x$ catalyts for their good performance of flue gas denitration.

2. Experimental section

2.1. Catalyst preparation

Raw materials used for TiO_2–SiO_2 preparation included blast furnace slag (BFS), titanium(IV) chloride ($TiCl_4$) and colloidal silica (30 wt% SiO_2 in water), or tetrabutyl titanate ($Ti(OC_4H_9)_4$) and tetraethyl orthosilicate ($Si(OC_2H_5)_4$). The BFS was water-quenched slag and from Panzhihua Iron & Steel Group Co., Ltd of China. Table 1 shows its composition obtained by XRF analysis. All other chemicals were all commercial products of reagent grade (Alfa Aesar). For comparison, a kind of commercial V–W–Ti SCR catalyst denoted as DKC ZERONOX® 993510537 was gotten from Chengdu Dongfang KWH Environmental Protection Catalyst Co., Ltd., China. This commercial monolithic honeycomb catalyst was crushed into powder and further evaluated to compare with the prepared catalysts.

The TiO_2–SiO_2 supports used in making $DeNO_x$ catalysts were prepared from different precursors according to the technical routes shown in Fig. S1 (see ESI†). The first support denoted as S-BFS-1 was prepared from BFS by, in succession, digesting the slag in 70 wt% H_2SO_4 at 90 °C for 3 h; hydrolyzing the resulting solution containing $TiOSO_4$/Si at pH = 1 and 110 °C for 5 h, washing the obtained H_2TiO_3 slurry using H_2O, aqueous NH_3 (10 wt%) and H_2O again, and finally drying the filter cake to obtain the TiO_2–SiO_2 support. The second BFS-based support with different amounts of Al_2O_3/Fe_2O_3/SO_4^{2-} dopants (S-BFS-2) was obtained *via* a similar procedure but its slag digestion used 60 wt% of H_2SO_4, hydrolysis did not have any pH adjustment and slurry washing to pH = 7 by using only distilled water. The detailed procedure for preparing the BFS-based supports can be found in our previous publications.[17,24]

Commercial Ti and Si precursors were also used to synthesize TiO_2–SiO_2 by co-precipitation and sol–gel methods. Following literature reports,[28,29] $TiCl_4$ and colloidal silica were used in co-precipitation, and the resulting precipitate was washed with distilled water and aqueous NH_3 to get S-CP-$TiCl_4$. Another TiO_2–SiO_2 support (S-SG-Organic) was made by sol–gel method from $Ti(OC_4H_9)_4$ and $Si(OC_2H_5)_4$ precursors.[5,30] All samples had the similar SiO_2 content and were calcined at 600 °C for 4 h in air to obtain catalyst supports.

Table 1 Chemical composition of blast furnace slag (mass%)

TiO_2	SiO_2	MgO	CaO	Al_2O_3	Fe_2O_3	SO_4^{2-}	Others	Particle size
20.87	23.18	10.32	26.96	13.83	1.36	1.67	1.81	<0.2 mm

With the preceding TiO_2–SiO_2 supports, all $DeNO_x$ catalysts were obtained by impregnating 5 wt% WO_3 and 2 wt% V_2O_5. The impregnation slurry was continuously stirred at 60 °C until it became a paste. Then the paste was dried at 110 °C for 10 h and calcined at 600 °C for 4 h to get the V_2O_5–WO_3/TiO_2–SiO_2 catalysts.[24] Four catalysts were prepared and denoted as BFS-1, BFS-2, CP-$TiCl_4$ and SG-Organic according to their different raw materials and synthesis methods used in preparing the TiO_2–SiO_2 supports.

2.2. Characterization and evaluation

Nitrogen adsorption/desorption isotherms were obtained using an ASAP 2020 (Micromeritics Instrument Corp.) working at 77 K. For all samples measured, they were degassed in vacuum at 150 °C for 6 h in prior to BET measurement. The Brunauer–Emmett–Teller (BET) equation was used to calculate the specific surface area (S_{BET}) from the recorded isotherms. Pore size distribution was calculated from the adsorption curve using the Barrett–Joyner–Halenda (BJH) model. The nitrogen adsorption volume at a relative pressure (P/P_o) of 0.994 was adopted in determining the pore volume and average pore size. The X-ray diffraction (XRD) pattern was performed in the 2θ angle from 10° to 90° on a D/Max-RB diffractometer (Rigaku Corp., Tokyo, Japan) having a Cu Kα radiation. FT-IR spectra were taken using a Tensor 27 (Bruker, Germany) in 400–4000 cm^{-1} with a resolution of 4 cm^{-1}. For this, 1.0 mg dry powder was dispersed into 100 mg *IR* transmissive material (KBr), which was further pressed to obtain the transparent disks used for measurement.

The bulk chemical composition of blast furnace slag and all the prepared supports were determined in an Axios X-ray fluorescence (XRF) spectrometer (PANalytical X'pert). The composition and oxidation state of elements presented on the surface of prepared catalysts were obtained using a X-ray photoelectron spectroscopy (XPS) working on an ESCALAB 250Xi electron spectrometer from Thermo Fisher Scientific Corporation (USA) using 100 W Al Kα radiation ($h\nu$ = 1486.6 eV). A catalyst sample was put into its sample holder in advance and further degassed overnight at room temperature at a pressure of 10^{-9} mbar. Binding energies were corrected by referring to the binding energy 284.8 eV for C 1s. For all samples not containing carbon, such a C 1s signal in XPS spectra was from their adventitious carbon.

Surface morphology and cross-sectional structure of all prepared supports were characterized using a JSM-7001F scanning electron microscopy (SEM) of JEOL (Japan) working at an accelerating voltage of 10 kV, and further a JEM-2100 transmission electron microscopy (TEM) of JEOL working at 200 kV. All TEM samples were on a copper-supported carbon polymer grid, and a sample was formed by placing a few droplets (onto the grid) of a suspension made by dispersing ground sample into ethanol and in turn drying the droplets in room condition. The bulk and surface compositions of vanadium element in catalysts were determined using the Inductively Coupled

Plasma-Optical Emission Spectrometry (ICP-OES, ICAP 6300, USA) and Energy Dispersive X-ray Spectroscopy (EDS) attached to a JSM-7001F SEM, respectively.

Thermogravimetry (TG) coupled with differential scanning calorimetry (DSC) was conducted on a Labsys Evo STA 1600 (Setaram Instrumentation) to characterize the weight change and endothermal–exothermal characteristics of TiO_2-based supports and catalysts. The heating curves (TG/DSC) were recorded under inert atmosphere of argon at a heating rate of 10 °C min^{-1} in the range of 30–1000 °C. The presence of sulfate species in the sample was evaluated from the weight loss in the range in which the release of SO_2 occurred. Both NH_3-TPD and H_2-TPR experiments were performed on an AutoChem II-2920s V5.02 equipment (Micromeritics Instrument Corp.) to obtain the surface acidity and redox properties of a sample. After loading 0.1 g sample into its quartz U-tube reactor and purged with He, the sample was heated from room temperature to 300 °C at 10 °C min^{-1} and maintained at this temperature for 60 min in He. Then, the sample was cooled to 80 °C, followed by NH_3 adsorption for 1 h (10 vol% NH_3 in He), and finally heated to 600 °C at 10 °C min to obtain NH_3-TPD curve in 50 mL min^{-1} pure He. For H_2-TPR analysis the sample was cooled to 90 °C and followed by heating it to 1000 °C at 20 °C min^{-1} in H_2–He (10 vol% H_2) gas at 50 mL min^{-1}. The released NH_3 or consumed H_2 were continuously detected using a mass spectrometer (Proline MS, Ametek).

Catalytic activity for SCR of NO by NH_3 was evaluated in an atmospheric quartz fixed bed reactor of 15 mm in internal diameter. The tested catalyst was powder of 0.15–0.2 mm in sizes, and the used simulated flue gas contained 0.06 vol% NO, 0.048 vol% NH_3, 3 vol% O_2, 5 vol% H_2O, 0.06 vol% SO_2, and balanced with N_2. The tested model flue gases included NO–O_2–N_2, NO–O_2–H_2O–N_2 and NO–O_2–H_2O–SO_2–N_2, and for each kind of gas its total flow rate through the reactor was kept at 400 mL min^{-1} (STP) to give a high Gas Hourly Space Velocity (GHSV) of 100 000 h^{-1}. The tested reaction temperature was in 150–500 °C and under each condition the test was last for 60 min. Molar concentrations for feeding and reacted gases were continually monitored in an ABB-AO2020 on-line flue gas analyzer (ABB). The realized NO conversion was calculated according to the measured inlet and outlet NO concentrations by

$$\text{NO conversion } (\%) = \frac{NO_{in} - NO_{out}}{NO_{in}} \times 100.$$

3. Results and discussion

3.1. Characterization of TiO_2–SiO_2 supports

XRF analysis. Table 2 shows the chemical compositions of all TiO_2–SiO_2 supports. Their SiO_2 content was all about 9.3 wt%, but the slag-based samples contained some unavoidable dopants such as Fe_2O_3, Al_2O_3 and SO_4^{2-}. With controlled hydrolytic pH and aqueous NH_3 washing (10 wt%), the S-BFS-1 support contained 1.38% Fe_2O_3, 0.59% Al_2O_3 and 0.39% SO_4^{2-}, whereas S-BFS-2 prepared without aqueous NH_3 washing had significantly less Fe_2O_3 (0.31%) and Al_2O_3 (nearly zero) but more SO_4^{2-}. This amount variation for Fe_2O_3 and Al_2O_3 dopants in a slag-based samples were subject to the solubility of such species in hydrolytic solution with a certain pH value.[31,32] Both S-CP-$TiCl_4$ and S-SG-Organic samples contained only TiO_2 and SiO_2.

Table 2 Chemical composition of TiO_2–SiO_2 supports determined by XRF analysis

Support	TiO_2	SiO_2	Fe_2O_3	Al_2O_3	SO_4^{2-}	Others
S-BFS-1	87.72	9.17	1.38	0.59	0.39	0.75
S-BFS-2	87.18	9.3	0.31	—	2.97	0.24
S-CP-$TiCl_4$	90.67	9.21	—	—	0.12	—
S-SG-Organic	90.72	9.28	—	—	—	—

Textural characteristics. Fig. 1 and Table 3 show the results of BET analysis for all supports. Fig. 1 shows the obvious difference for all supports in the N_2 adsorption/desorption isotherms and pore size distribution (PSDs) curves. All supports exhibit irregular pore shape and type-IV isotherms in Fig. 1a (IUPAC classification) to characterize the mesoporous feature.[33,34] Both SiO_2 and other oxide dopants like Al_2O_3, Fe_2O_3 caused S-BFS-1 to have mesoporous structure with high BET area (282.30 m^2 g^{-1}) and high pore volume (0.609 cm^3 g^{-1}). For S-BFS-2, its high SO_4^{2-} content and low Al_2O_3 and Fe_2O_3 contents led to the meso–macro PSDs having lowered surface area (137.91 m^2 g^{-1}) and pore volume (0.293 cm^3 g^{-1}). The large mesopores and even macropores in 20–100 nm on S-BFS-2 might be from the packing of secondary aggregates.[28] Also, the crystalline size detected by XRD obviously increased from 11.9 nm for S-BFS-1 to 16.6 nm for S-BFS-2. All these indicated that the Al_2O_3 and Fe_2O_3 dopants possibly prohibited aggregation of crystallites to resist the reduction in surface area during high-temperature calcination and thus facilitated the formation of highly mesoporous structure.[4,8,35] However, the presence of SO_4^{2-} worked oppositely. Literature reviews[8,30,33] showed that the titania catalysts with high specific surface areas are well suited for selective catalysis because of their more available active sites. For S-CP-$TiCl_4$ and S-SG-Organic made using commercial reagents (without Al_2O_3 and Fe_2O_3 dopants), they had lowered BET area and pore volume in comparison with S-BFS-1, although S-BFS-1 had more sulfate. Especially for S-CP-$TiCl_4$ (made with the similar method as for S-BFS-1), it had the much smaller BET surface area, pore volume and pore size. Thus, there are great advantages for preparing high-surface-area TiO_2–SiO_2 supports from BFS.

XRD analysis. The XRD patterns compared in Fig. 2 show that TiO_2 in all supports presents as anatase crystal form (JCPDS 21-1272).[5,35,36] Estimation according to the Scherrer's formula based on the (101) diffraction peak found that the anatase crystallites are in sizes of 11.3–16.6 nm (see Table 3). Of them, the crystallite size of S-BFS-1 (containing Al_2O_3/Fe_2O_3 dopants) is about 11.3 nm, very close to that of pure TiO_2–SiO_2 made with organic materials. The sulfate in S-BFS-2, however, caused a slight growth of titania crystallinity to have thus its reduced BET surface area and big crystallite size, as similarly reported by M. Kobayashi *et al.*[37] Overall, the supports from

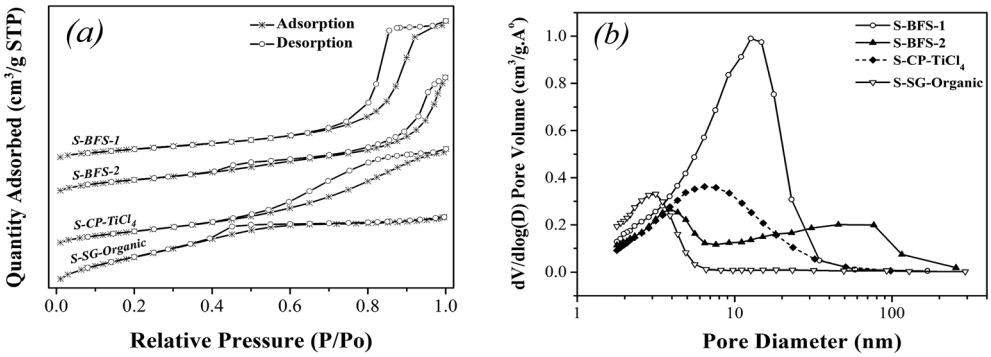

Fig. 1 Nitrogen adsorption/desorption isotherms (a) and pore size distribution (b) of TiO_2–SiO_2 supports.

BFS had high crystallinity than the samples made with organic precursors did, possibly due to the heat intolerance in calcination of the latter.[38] Thus, the origin (nature) of precursor and preparation procedure affected the crystallization characteristics of TiO_2.

Thermal analysis. Fig. 3 shows the TG and DSC profiles of calcined TiO_2–SiO_2 supports in a temperature range of 30–1000 °C with a heating rate of 10 °C min^{-1} in argon. The thermal event at 30–200 °C can be correlated to the DSC endothermic peak at around 100 °C to indicate the removal of physically adsorbed water.[31,39,40] There was not obvious weight loss and an exothermic peak when further increasing temperature to 600 °C, indicating the completion of amorphous-anatase phase transformation for all supports and there was not organic matters trapped inside the pores of S-SG-Organic.[36,41] Comparing S-BFS-1, S-CP-$TiCl_4$ and S-SG-Organic, the TG diagram of S-BFS-2 had a distinctively big weight loss peak in 550–800 °C to show the decomposition of sulfate species (see Table 2).[39,40] Besides, the DSC heating curves in 600–1000 °C revealed that varying the transition point of anatase to rutile due to the introduction of dopants showed a influence of dopants on kinetics of anatase-to-rutile transformation taking place *via* changes of oxygen vacancies in a support.[42]

SEM images. Fig. 4 displays SEM (also TEM) micrographs of all support samples. In Fig. 4a–d (SEM), all synthesized TiO_2–SiO_2 supports possess a rough porous surface, and the samples S-BFS-1 (a), S-CP-$TiCl_4$ (c) and S-SG-Organic (d) show shaped agglomerates composed of asymmetric plate-like particles. The S-BFS-2 (b) exhibits micro spherical morphology with heavy aggregation, possibly from breakage of its structure into small pieces of matters in sintering due to its high sulfate content.[43] For slag-based supports containing unavoidable Fe_2O_3 dopant, one can see a dense elemental distribution of Ti in their SEM images and EDS mappings of Ti and Fe shown in Fig. S2 and S3 (ESI†). This reveals the presence of underlying TiO_2 substrate and uniform Fe dispersion on the entire TiO_2 substrate. Their

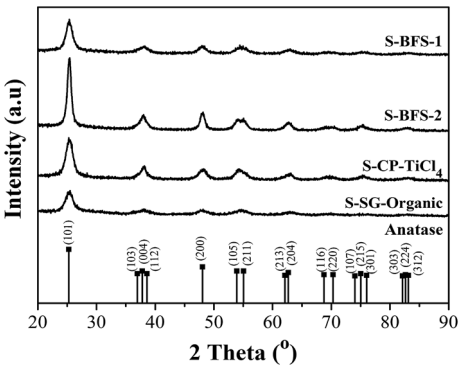

Fig. 2 XRD patterns of TiO_2–SiO_2 supports.

Table 3 Textural parameters of TiO_2–SiO_2 supports calcined at 600 °C and elemental composition of their catalysts

	Textural properties of support				Elemental composition of catalyst					
					Elemental bulk composition (ICP)[b]			Elemental surface composition (EDS)[c]		
Sample	BET (m^2 g^{-1})	Pore size (nm)	Pore volume (cm^3 g^{-1})	Crystallite size[a] (nm)	V	Ti	V/Ti	V	Ti	V/Ti
S-BFS-1	282.30	8.62	0.609	11.9	1.151	47.17	2.44	1.72	41.14	4.18
S-BFS-2	137.91	8.50	0.293	16.6	1.147	45.68	2.51	0.93	45.2	2.06
S-CP-$TiCl_4$	164.07	6.95	0.285	13.48	1.125	46.18	2.44	1.65	57.36	2.88
S-SG-Organic	150.66	3.04	0.114	11.30	1.161	48.23	2.41	1.73	60.94	2.85

[a] Crystallite size of TiO_2 was calculated from X-ray diffraction (XRD) data. [b] Actual bulk concentration was obtained by inductively coupled plasma (ICP). [c] Surface composition was obtained from energy dispersive X-ray spectroscopy (EDS) attached to SEM.

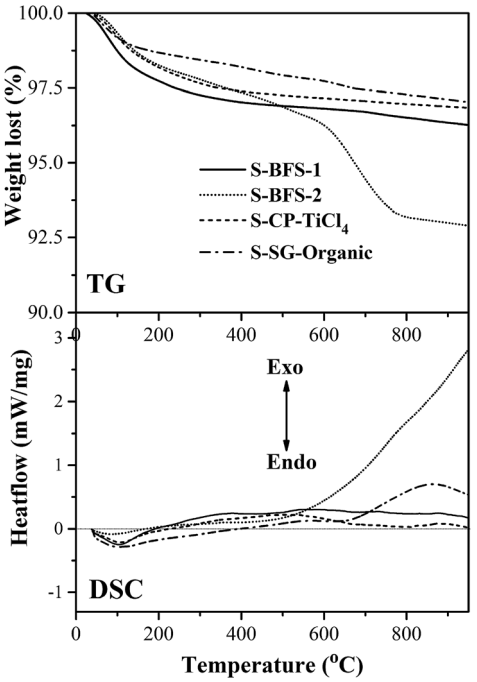

Fig. 3 TG and DSC profiles of TiO_2–SiO_2 supports at a heating rate of 10 °C min^{-1} (in argon).

EDS spectra further suggested that the ferric elements were not aggregated, complying with the absence of Fe_2O_3 peak in XRD patterns shown in Fig. 2.[13,14] Both S-CP-$TiCl_4$ and S-BFS-1, prepared *via* the same co-precipitation method, displayed the similar morphology to indicate that starting material has not obvious effect on morphology of the resulting support. Overall, the surface morphology of synthesized support obviously varied with the treatment method, either co-precipitation or sol–gel synthesis. The particles from sol–gel method (S-SG-Organic) showed some layered stacking structure with less rough surface than the co-precipitation method did.[44]

TEM images. As shown by TEM images in Fig. 4e–h, all TiO_2–SiO_2 supports had spherical primary particles without any coating on surface.[31] Mesopore structure features can be clearly seen to indicate high surface area and high adsorptive capacity.[35,38] The S-BFS-1 had the best dispersion to show small particle sizes, while serious aggregation occurred to S-BFS-2 to form large particle sizes. The results well agree with the BET results in Fig. 1. For all samples, SiO_2 particles and impurities were not clearly identified and their non-uniform distributions were observed in the TEM images. A high-resolution transmission electron microscopic study (HR-TEM) was performed to observe the distribution of crystalline titania (Fig. S2–S5(a) in ESI†). All the observed lattice fringes of TiO_2–SiO_2 nanoparticles show a *d*-spacing of 0.360 nm, just corresponding to the (101) lattice fringes of anatase TiO_2 (d = 0.352 nm, JCPDS No. 21-1272).[35,38] In summary, one can see from the TEM and SEM images that the dopants and synthetic route remarkably affected the morphologies and nano-micron structure of the prepared TiO_2–SiO_2 supports, and the S-BFS-1 support had the best dispersion of its precursors.

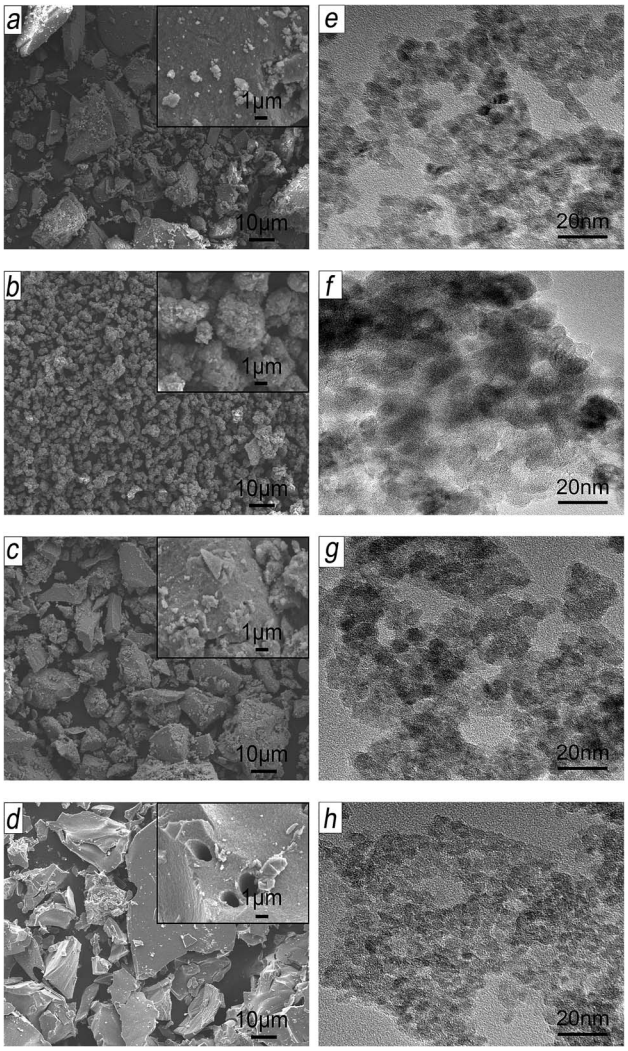

Fig. 4 SEM and TEM images of S-BFS-1 (a, e), S-BFS-2 (b, f), S-CP-$TiCl_4$ (c, g) and S-SG-Organic (d, h).

FT-IR analysis. The FT-IR spectra in Fig. 5 for all supports demonstrate a large and intense band within 3200–3600 cm^{-1} to indicate the presence of OH group on TiO_2–SiO_2 surface and also a sharp peak at 1635 cm^{-1} to refer to the O–H stretching vibration in water. The broad adsorption peak located in 400–

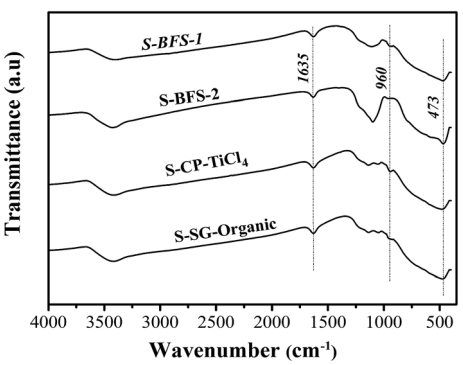

Fig. 5 FTIR spectra of TiO_2–SiO_2 supports.

600 cm^{-1} represents the characteristic vibration of Ti–O bonds in Ti–O–Ti.[5,35,45] An absorption band extending from 1000 to 1300 cm^{-1} shows the asymmetric and symmetric stretching of Si–O–Si bridge, and a minor feature around 960 cm^{-1} can be associated with the vibrations of Si–O–Ti linkage. Thus, a substitution of Si for Ti has occurred in the prepared TiO_2–SiO_2 supports.[35,45] Besides, the absorption band within 1000–1300 cm^{-1} is more intensive for the sulfated S-BFS-2 sample, indicating the vibration overlapping of Si–O–Si and S=O bonds, where the latter is associated with sulfate groups and anchored to TiO_2–SiO_2 surface.[39,46]

In summary, the supports made with the co-precipitation method, as compared to the sol–gel synthesis, displayed the similar morphological features and their rough porous surface provided the larger surface area. On the other hand, the dopants also greatly influenced the structure of synthesized TiO_2–SiO_2 such as size of crystallites, porous textures and particle agglomeration. The dopants Al_2O_3 and Fe_2O_3 (as in S-BFS-1) facilitated mesoporous structure, enlarged BET surface area as well as mesoporous size because they inhibited the growth of anatase TiO_2 grain by their existence on TiO_2 boundary. The presence of SO_4^{2-} made the TiO_2–SiO_2 support easy to agglomerate to form meso–macro pores, having thus the obviously low surface area for S-BFS-2. These difference in porosity, surface area and crystallinity parameters of TiO_2–SiO_2 supports will greatly impact the catalysts made with them for SCR of NO with NH_3 (flue gas $DeNO_x$).

3.2. Evaluation of catalysts for $DeNO_x$

Denitration catalysts were prepared by impregnated 2 wt% V_2O_5 and 5 wt% WO_3 onto the preceding TiO_2–SiO_2 supports having different structures, properties and $Fe_2O_3/Al_2O_3/SO_4^{2-}$ dopants amounts. The SEM images and EDS spectra as well as mappings of Ti/V elements in Fig. S2–S5(b–e) shown in ESI† confirmed that all prepared V_2O_5–WO_3/TiO_2–SiO_2 catalysts were composed of Ti, Si, Al, Fe, O, V, W elements, and the main active element V was highly dispersed into the lattice of entire TiO_2 substrate.[14] The ICP-OES and EDS results shown that all the catalysts had the similar bulk vanadium contents of about 1.1 wt% but different surface V concentrations (Table 3), showing essentially the varied interactions between V_2O_5 and support for different catalysts.[13,14] In the following, $DeNO_x$ performance was evaluated to correlate the structure and dopants of supports with the catalytic performance for SCR of NO by NH_3.

Fig. 6 shows the results of $DeNO_x$ performance over catalysts prepared using the preceding supports. At the same reaction conditions, all prepared catalysts except for BFS-2 enabled higher NO reduction than the reference DKC commercial catalyst did in the reaction temperature of 250–450 °C. The realized NO removal over DKC below 70% but it had a acceptably wide temperature window for $DeNO_x$. The BFS-1 catalyst exhibited the best catalytic activity by having about 74% NO conversion in 300–450 °C under an NH_3/NO ratio of 0.8 and GHSV of 100 000 h^{-1}. The manifested activity for CP-$TiCl_4$ was between BFS-1 and SG-Organic catalysts. Although BFS-2 contained the highest sulfate, it showed the lowest activity among

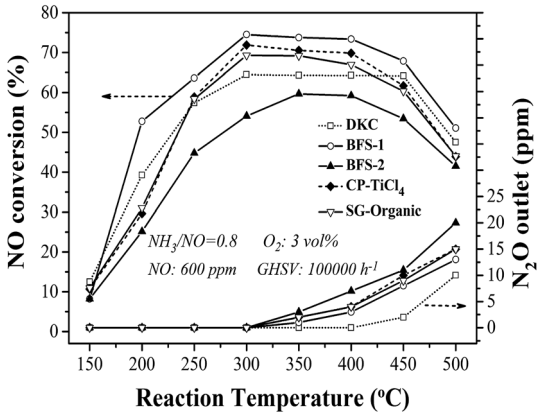

Fig. 6 NO conversion and N_2O formation varying with reaction temperature for prepared and commercial DKC catalysts.

all prepared catalysts. Referring to the support compositions in Table 2, one can conclude that the proper amounts of Fe_2O_3 and Al_2O_3 dopants in catalytic support facilitated NH_3-SCR reactions over V_2O_5–WO_3/TiO_2–SiO_2 catalysts. Earlier studies have shown that the incorporation of Al_2O_3 (ref. 20, 21 and 47) of up to 10 wt% and Fe_2O_3 (ref. 4, 11 and 48) of up to 3 wt% into the TiO_2 support are beneficial to NO reduction in NH_3-SCR, and the catalyst has better thermal stability in comparison with conventional V_2O_5/TiO_2 catalysts. Thus S-BFS-1 support should be a promising candidate for making inexpensive and highly active catalyst for flue gas $DeNO_x$. Also, one can infer that the activity for $DeNO_x$ of TiO_2–SiO_2 supported catalysts was mainly subject to the dopants in support other than the precursors (materials) and preparation method. The presence of Fe_2O_3 (ref. 4 and 11) and Al_2O_3 (ref. 20 and 21) would positively work on $DeNO_x$ performance of the resulting catalyst, but too much SO_4^{2-} (about 3 wt%) in support would lead to adverse impacts. Literature studies[37,49,50] have reported that the presence of about 1 wt% sulfate in TiO_2 and TiO_2–SiO_2 supports would promote NH_3-SCR performance of the resulting catalyst because of its increase in catalyst acidity and facilitation in oxidation of NO into nitrate and transformation of monomeric vanadate into polymeric vanadate on catalyst surface.

The generation of N_2O during NH_3-SCR was also tested. At temperatures above 350 °C, ammonia would be partially oxidized to N_2O,[3,7] but only negligible N_2O (3 ppm) was formed at 450 °C over DKC (see Fig. 6). The formed N_2O amount at 350–500 °C over all catalysts followed a sequence of BFS-2 > CP-$TiCl_4$ ≈ SG-Organic > BFS-1 > DKC. In term of composition and structure features, the low emission of N_2O at high temperatures over BFS-1 catalyst should be related to its presence of Al_2O_3 and Fe_2O_3 dopants. Hence, the type of dopants is critical to achieve the expected high N_2 selectivity of catalyst for SCR of NO by NH_3.

The tolerance to poisoning of SO_2 and steam was tested by feeding 5 vol% steam and 600 ppm SO_2 at 300 °C in a stable SCR reaction lasting for a few hours under GHSV of 100 000 h^{-1}. As shown in Fig. 7, the presence of both SO_2 and H_2O in the reactant (fed) gas caused obvious loss of $DeNO_x$ activity from the case with only H_2O (steam) feed. Having only 5 vol% H_2O in gas

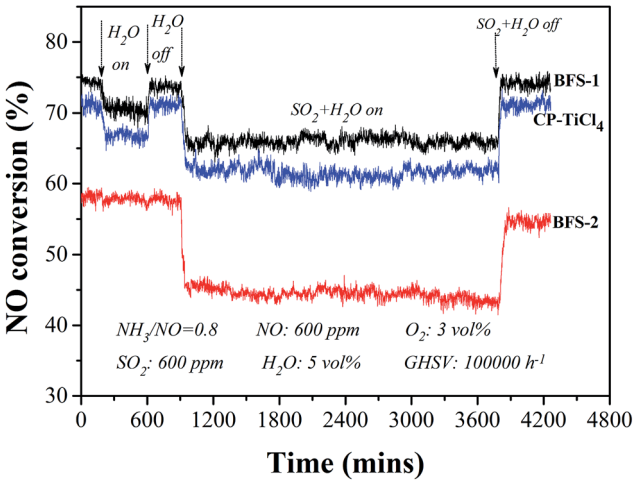

Fig. 7 Stability tests of BFS-1, BFS-2 and CP-$TiCl_4$ catalysts for SCR of NO by NH_3 at 300 °C.

the absolute drop of NO conversion was 2.6%, 3.5% respectively over the BFS-1, CP-$TiCl_4$ catalysts, meanwhile the deactivation nearly was not seen over sulfated TiO_2–SiO_2 supported catalyst (BFS-2). The interaction of sulfate species with adsorbed water can cause the formation of Brønsted acid sites to promote the NH_3 adsorption, which may compensate the degree of the loss of its $DeNO_x$ efficiency.[39,51] Stopping H_2O feed, NO conversions were fully reversible for all catalysts, indicating that this inhibition is due to competitive adsorption of H_2O and NH_3 on active sites.[1,46]

Feeding SO_2 and steam simultaneously revealed that the realized NO conversion was stable but further dropped by 8%, 10% respectively for BFS-1 and CP-$TiCl_4$ catalysts from the flue gas without presence of SO_2 and steam, furthermore shutting off the feeding of both SO_2 and steam, their $DeNO_x$ activity were recovered quickly to their initial high value. At the analogous reaction conditions, the activity over BFS-2 dropped by 12.7% and decreased gradually afterwards, besides its recovery of catalytic performance was gradual and the performance could not rebound to the original after cutting off SO_2 and steam in fed gas. Thus, high sulfate content in catalyst is not good for tolerance to the poisoning of steam and SO_2 because the formed Brønsted acid sites and long-term exposure to SO_2 containing in flue gas can lead to the formation of ammonium sulfates (NH_4HSO_4 and $(NH_4)_2SO_4$) on catalysts easily,[1,2,30,46] which would cause similar deactivation for all catalysts. In summary, the impurities Al_2O_3/Fe_2O_3 (excluding SO_4^{2-}) not only enhanced $DeNO_x$ activity and selectivity of the prepared catalyst but also positively affected the resistance of the catalyst to poisoning by water and SO_2 in SCR of NO.[20,52] Obviously, BFS-1 is the most active and robust catalyst for $DeNO_x$ application to actual flue gases.

Correlating with structure of catalyst supports found that the preceding catalytic activities for $DeNO_x$ increased with increasing the surface area of supports. Indeed, large pore volume and high surface area of a catalyst would improve its catalytic activity by facilitating spread of reactant molecules (NO) or reaction intermediates to active sites in catalyst's mesostructure framework.[30,33,53] The catalyst BFS-1 showed high NO reduction capability (about 74% reduction) at 300–450 °C under high GHSV of 100 000 h^{-1}. Agglomeration observed on BFS-2 reduced its BET surface and also blocked some active sites, which caused thus the instability of the catalyst in gas containing both of steam and SO_2.[43] Thus, the texture and morphology of support importantly affect the catalytic performance of V_2O_5–WO_3/TiO_2–SiO_2 for $DeNO_x$ by NH_3. The BFS-1 catalyst with the relatively low crystallinity exhibited the best $DeNO_x$ activity, possibly owing to its special acid sites and large BET surface area to have highly dispersed vanadia on catalyst surface, as further justified below.

3.3. Justification of catalytic activities

NH_3-TPD. Comparing the profiles of temperature programmed desorption of ammonia (NH_3-TPD) in Fig. 8 shows clearly different acidic sites for catalysts having different contents of $Al_2O_3/Fe_2O_3/SO_4^{2-}$ dopants. While BFS-2 containing high SO_4^{2-} content displayed two broad NH_3 desorption regions below and above 400 °C to refer to weak and strong acid sites, the other catalysts exhibited only one broad and asymmetric peak below 400 °C to represent weak acid sites.[20,35,45] The clarification in Fig. 8 and data in Table 4 show actually that the impurities in slag-based catalysts caused strong acidic sites on catalyst surface in comparison with those prepared from commercial Ti/Si sources. The highest amount of desorbed NH_3 occurred at temperatures of 100–400 °C for BFS-1. For BFS-2 its strong acidic sites occurred at 400–600 °C due to the strong interaction between sulfate anion and titanium cation which causes the titanium cation to be more positively charged ions. Accordingly there were few weak acid sites for BFS-2, showing that the strong acid sites are formed by reducing weak acid sites,[8,54] causing strong adsorption and oxidation of NH_3 to hinder the SCR reaction for NO as evidenced in Fig. 6.[7,37,49] Weak acidic sites are beneficial to $DeNO_x$ activity by their retaining of NH_3 for SCR reaction.[5,7,36] This was confirmed by correlating the $DeNO_x$ activity and amount of weak acid sites such that BFS-1 had the highest amount of weak acid sites and also the best $DeNO_x$ performance. The presence of unavoidable sulfate species in CP-$TiCl_4$ prepared by co-precipitation using H_2SO_4

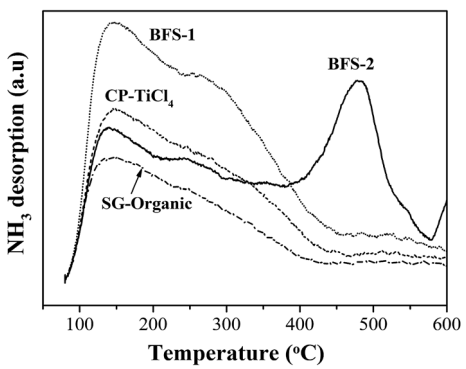

Fig. 8 TPD profile of NH_3 on V_2O_5–WO_3/TiO_2–SiO_2 catalysts.

Table 4 Results of NH_3-TPD and H_2-TPR experiments for all prepared $DeNO_x$ catalysts

	Acidity: NH_3 desorption (mmol g^{-1})			Redox properties: H_2 consumption (mmol g^{-1})		
Catalyst	Weak acid	Strong acid	Total	VO_x reduction	WO_x reduction	Total
BFS-1	0.317	—	0.317	0.316	0.126	0.442
BFS-2	0.073	0.075	0.148	0.299	0.071	0.370
CP-$TiCl_4$	0.210	—	0.210	0.158	0.169	0.327
SG-Organic	0.139	—	0.139	0.122	0.067	0.189

acid caused more adsorbed NH_3 to participate in SCR reaction and had thus higher NO_x reduction than SG-Organic catalyst did. In summary, the difference in $DeNO_x$ activity for all compared catalysts having the same SiO_2 content should be correlative with their different weak acidities that determine the ability to retain adsorbed NH_3.[5,36] For S-BFS-1, its high BET surface area acquired from its Al_2O_3/Fe_2O_3 dopants and proper sulfate content (0.4 wt%) caused the catalyst to have abundant weak acid sites and thus good $DeNO_x$ performance. The too much SO_4^{2-} in support can convert a part of weak acid sites into inert strong acidic sites to decrease $DeNO_x$ activity as S-BFS-2 performed.[7,37]

H_2-TPR. Fig. 9 shows the H_2-TPR diagrams for all catalysts, and their corresponding amounts of consumed H_2 were summarized in Table 4. A two-step reduction profile was observed with their T_{max} at 431–471 °C and 718–863 °C and representations of active V_2O_5 and promoter WO_3, respectively.[3–5] The samples made from slag exhibited the larger reduction peak, indicating the more reducible metal oxides on catalyst surface or the higher reducibility for slag-based catalysts.[3,5,55] On the other hand, the shift of reduction peak for active VO_x reflects the difficulty in changing its valence during $DeNO_x$ reactions.[5,36] The lower reduction temperature of VO_x species, the higher catalytic activity was achieved.[3,5] For BFS-1, it had the lowest T_{max} to reduce VO_x species and the highest H_2 consumption in H_2-TPR, indicating its more reducible active VO_x species and thus higher $DeNO_x$ efficiency clarified in Fig. 6. In comparison, the BFS-2 catalyst with the highest T_{max} for reducing VO_x species manifested the worst $DeNO_x$ performance so that CP-$TiCl_4$ and SG-Organic catalysts had the intermediate catalytic activity for $DeNO_x$ to respond their intermediate T_{max} for reducing VO_x species. Considering its high BET surface area, the low reduction temperature and many reducible sites for BFS-1 may be owing to its highly dispersed VO_x species on catalyst surface.[8,30,33]

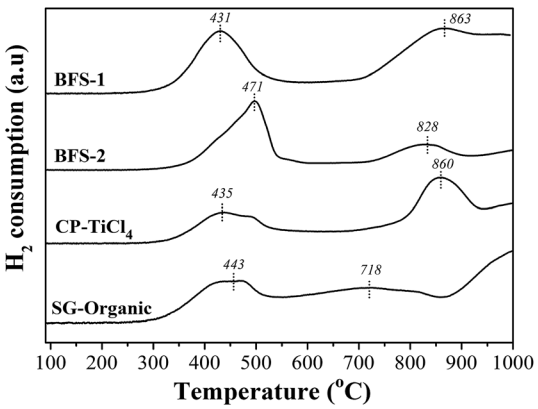

Fig. 9 H_2-TPR profile of V_2O_5–WO_3/TiO_2–SiO_2 catalysts.

XPS. Fig. 10a–d show the electron binding energies of Ti 2p, Si 2p, O 1s and V 2p XPS peaks of V_2O_5–WO_3/TiO_2–SiO_2 catalysts determined using XPS analysis. All peaks were fitted by Gaussian–Lorentz curves. One may see that the reported electron binding energies agree well with other reports.[5,25,26,35,45,56] From the XPS spectra of Ti 2p in Fig. 10a we can see that the binding energies (BE) of Ti $2p_{3/2}$ and Ti $2p_{1/2}$ refer to Ti^{4+} in TiO_2, which are respectively higher than 458.7 and 464.4 eV for pure TiO_2.[5,35,45] A downward shift (to be slightly lower) of Si 2p BE was detected in Fig. 10b, as compared to 103.4 eV for pure SiO_2,[5,35] which indicates a decrease in the effective positive charge on Si. These essentially revealed the strong interaction between TiO_2 and SiO_2 in TiO_2–SiO_2 support. Since Ti has greater affinity to oxygen than Si does, some Si–O bands disappeared to promote the formation of Ti–O bands on surface and thus to reduce the binding energy of Si 2p. Combining the results of XPS and FT-IR (Fig. 5) suggests the formation of Ti–O–Si linkages in the prepared catalyst, as also reported elsewhere.[25,26] There were obvious upward shift of Ti 2p and downward shift of Si 2p for BFS-1 in comparison with the other three samples, referring to more Ti–O–Si linkages and better interspersion of Ti–Si components in this support. This well accounts for the high BET area, small particle size and weak crystallization for BFS-1.[7,25,26]

Fig. 10c shows interesting feature of O 1s XPS spectra. All catalysts are characterized by complex profiles to indicate the presence of different oxygen chemical bonds. The BE around 533 eV is attributed to the surface adsorbed oxygen (denoted as O_{ads}), such as O_2^{2-} or O^- belonging to defect-oxide or hydroxyl-like group. Another peak located around 530 eV corresponds to the lattice oxygen atom O^{2-} (denoted as O_{lat}), indicating a mainly single chemical environment surrounding the photo emitting oxygen.[25,26] Against the O_{lat} for catalyst based on pure TiO_2, the upward shifts in BE of O 1s peak for all other catalysts clarified a substitution of Ti atoms by other higher electronegativity elements like Si, Al, Fe, S.[5,25,26] For BFS-2, the upward shift of O 1s peak was more pronounced, as recognized from the broad O_{ads} peak, which reflects a more electronegative environment around oxygen atom due to the strong electron affinity by S^{6+} in SO_4^{2-}.

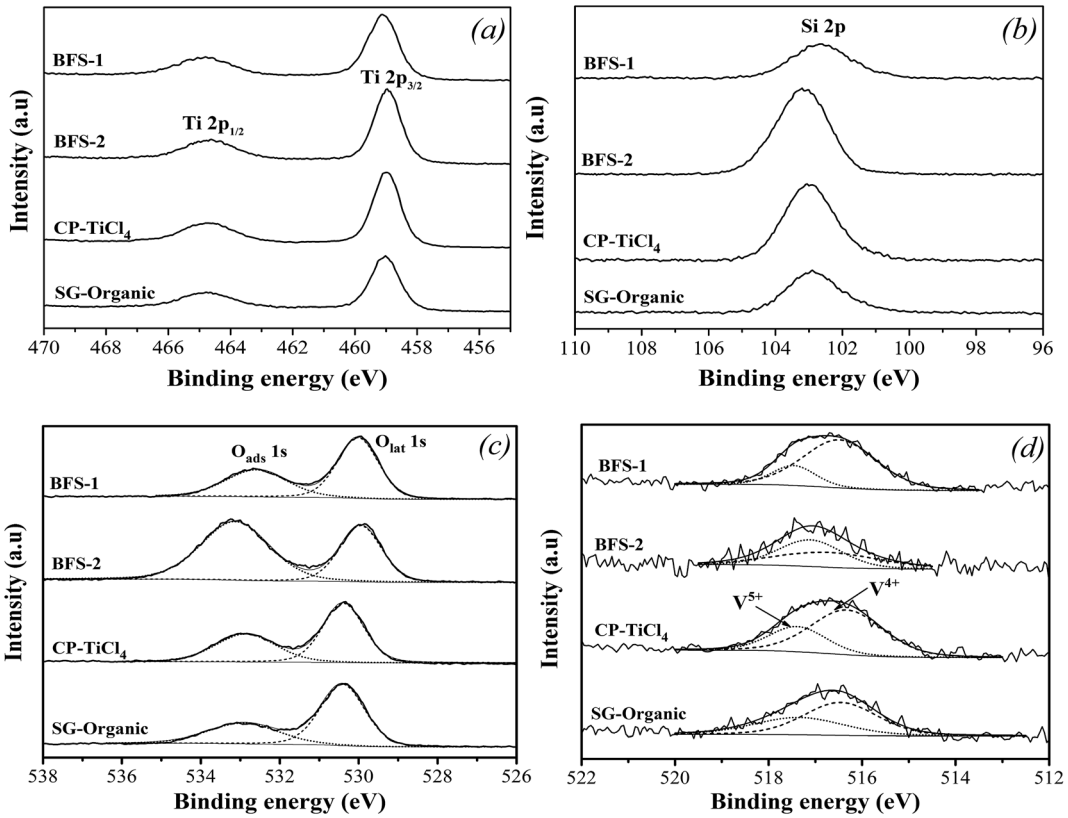

Fig. 10 XPS spectra of Ti 2p (a), Si 2p (b), O 1s (c) and V 2p (d) in TiO_2–SiO_2 based catalysts.

Table 5 shows the surface O_{ads}/O ratios of all samples. The slag-based catalysts had notably high O_{ads}/O ratios. The more O_{ads} on surface should result from the more defects created by the Al_2O_3, Fe_2O_3, SO_4^{2-} dopants. The O_{ads} is usually considered to be beneficial for NO oxidation into NO_2 in SCR reactions, thereby facilitating "fast SCR" reaction and enhancing $DeNO_x$ efficiency at low temperatures.[5,18] Thus, the more surface adsorbed oxygen O_{ads} should be responsible for the better catalytic performance of BFS-1. However, a very high O_{ads}/O ratio, such as for BFS-2, means an excessive oxidation ability, which is harmful to SCR reaction owing to its induced strong ammonia oxidation that forms nitrogen oxide byproducts to narrow the temperature window of SCR and to generate more N_2O (Fig. 6).[56]

Table 5 Surface elemental composition (% atomic concentration) and atomic ratios of prepared catalysts

	Surface atomic concentration (at.%)					Surface atomic ratios[a], %	
Catalyst	Ti 2p	Si 2p	O 1s	V 2p	W 4f	O_{ads}/O	V^{4+}/V
BFS-1	22.28	9.86	64.78	0.82	2.26	48.24	80.37
BFS-2	13.18	19.09	66.26	0.24	1.23	63.02	48.89
CP-$TiCl_4$	20.63	11.26	65.51	0.68	1.93	40.96	69.15
SG-Organic	19.46	12.17	65.19	0.65	2.53	34.83	60.66

[a] Calculated from the ratio of peak area of XPS spectra.

The XPS spectra in Fig. 10d presents the chemical states of vanadium. In all prepared catalysts, two peaks representing V^{5+} and V^{4+} were detected in the range of 516.4–517.1 eV and 515.7–516.2 eV, respectively.[5,7] Table 5 listed surface atom concentrations and peak-fitting results of O 1s and V 2p spectra. We can see that BFS-1 had the highest surface V to indicate the best dispersion of vanadium species in the catalyst. Combining with the BET results in Fig. 1, the surface V signals are well related with the BET area of the four catalysts, meaning that high BET area is in favor of dispersion and exposure of vanadium species. Moreover, the non-stoichiometric V^{4+} species can improve the NO reduction ability of catalyst due to its high mobility and activation of electron transfer.[5,7,21] Consequently, the realized $DeNO_x$ efficiency for all catalysts are proportionally correlated with the amount of V^{4+} ratio on their surfaces shown in Table 5. The BFS-1 catalyst had the highest BET area, best dispersion of surface vanadium species and largest V^{4+}/V ratio, thus it was rich in active vanadium sites on its surface to ensure its good catalytic performance in SCR of NO. Furthermore, Table 3 shows that the surface V/Ti ratio of BFS-1, CP-$TiCl_4$ and SG-Organic catalysts were higher than their bulk ratios, suggesting that V_2O_5 was mainly dispersed on their catalyst surface. The surface V/Ti ratio of BFS-2 was lower than its bulk ratio, implying that its vanadium mainly existed in the inside of catalysts.[57] The BFS-2 catalyst had consequently poor $DeNO_x$ performance as was tested.

Spent catalyst analysis. Table 6 summarized the textural characteristics (S_{BET} and V_{pore}) of fresh and spent BFS-1, BFS-2 and CP-$TiCl_4$ catalysts, where the spent ones refer to 70 h

Table 6 Properties of spent catalysts after exposure to SO_2 and steam at 300 °C for 70 h

	Fresh catalysts		Spent catalysts			
Catalyst	Surface area (m^2 g^{-1})	Pore volume (cm^3 g^{-1})	Surface area (m^2 g^{-1})	Pore volume (cm^3 g^{-1})	TG loss in 250–550 °C (%)	TG loss for >550 °C (%)
BFS-1	144.86	0.436	133.64	0.409	—	3.6
BFS-2	115.63	0.290	90.22	0.218	4.0	7.5
CP-$TiCl_4$	136.42	0.270	121.43	0.232	—	3.8

exposure to SO_2 and steam at 250 °C. They all showed decrease in catalyst surface area, corresponding to the drop in catalytic activity when exposed to SO_2 and steam. There should be some solid materials formed during SCR reaction in flue gas containing SO_2 and H_2O, which blocks or collapses pores of catalyst.[2,22,30,33] The more decrease in pore volume would lead to more deactivation species deposited on catalyst.[2] There are two possible kinds of such deactivation species. The reaction between SO_2 or sulfate and NH_3 forms $(NH_4)_2SO_4$ and NH_4HSO_4 at low temperatures to block pores by deposition, while some active metal oxides may be sulfated by SO_2 to form stable sulfate species to destroy pore structure.[2,9,22,58]

The most serious poisoning suffering for BFS-2 in Fig. 7 was further verified by the high amount of sulfate existing on its spent catalyst (see TG data in Table 6). The weight loss at 250–550 °C represents the decomposition of ammonium sulfate salts,[22] which was observed only for spent BFS-2 catalyst. Considering its high SO_4^{2-} content and abundant strong acid sites in 400–600 °C shown by NH_3-TPD experiment, this catalyst is easier to accommodate irreversible ammonium salts during SCR of NO, which thus decreased catalyst lifetime and was hard to regenerate. The meso–macro PSDs of BFS-2 would also facilitate accommodation of ammonium salts during SCR.[58] For mesoporous BFS-1 and CP-$TiCl_4$ catalysts that had only weak acid sites, their ammonium salts in pores could be evaporated to greatly restore blocked pores and surfaces, thereby recovering their $DeNO_x$ activity after stopping the SO_2 and steam feed into the tested flue gas. The mass loss occurred at 500–850 °C provided an evidence for the sulfate ions incorporated into TiO_2 lattice (stable metal sulfates). This also decreased the pore volume of catalysts, especially for spent BFS-2, and suggested structure damage and irreversible deactivation of BFS-2 catalyst for SCR of NO.[9]

As a summary, we can see that all spent catalysts lost their surface area in comparison with their fresh catalysts due to the formation of sulfate salts, especially for BFS-2 catalyst. This is the primary reason for the irreversible deactivation of catalyst for SCR of NO. On the other hand, too much doped SO_4^{2-} in catalyst such as BFS-2 and too many strong acid sites would cause serious generation of ammonium sulfate species to block active sites and collapse pore structure of catalyst. With suitable content of SO_4^{2-} dopant (below 1 wt%) in BFS-1, it increased NH_3 adsorption capacity and surface O_{ads}/O ratio to improve the $DeNO_x$ performance.

4. Conclusions

Four V_2O_5–WO_3/TiO_2–SiO_2 samples with different amounts of $Al_2O_3/Fe_2O_3/SO_4^{2-}$ dopants prepared from blast furnace slag (BFS) containing Ti/Si and also commercial Ti/Si sources were characterized to reveal the relationship among performance, structure and preparation method of catalyst. Results shown that the BFS-based catalysts with proper amounts of $Al_2O_3/Fe_2O_3/SO_4^{2-}$ dopants exhibited excellent catalytic activity, selectivity and stability to ensure the high NO reduction capability (about 74% reduction) at temperatures of 300–450 °C and NH_3/NO ratio of 0.8. The performance is much better than that realized by the catalyst made by co-precipitation or sol–gel methods using commercial Ti/Si sources. Characterization demonstrated that the Al_2O_3/Fe_2O_3 dopants acquired from using BFS prevented agglomeration of Ti–Si composite oxides and facilitated the formation of abundant Ti–O–Si linkages that led to good interspersion of Ti–Si components and high surface area of the resulting TiO_2–SiO_2 support. Reflecting on catalyst, the high surface area of TiO_2–SiO_2 support facilitated dispersion of active surface vanadium species, lowered reduction temperature of vanadium oxides and provided sufficient weak acid sites to create enough active surface V sites for high NH_3 adsorption capacity and active catalytic activity in SCR of NO over the catalyst. On the other hand, the proper amount of $Al_2O_3/Fe_2O_3/SO_4^{2-}$ dopants in a catalyst can also create more defects in its TiO_2–SiO_2 support to generate adsorptive O (O_{ads} species) on the catalyst surface which is required for fast SCR reaction and high $DeNO_x$ efficiency. A small amount of SO_4^{2-} in catalyst would increase the weak acid sites and form proper O_{ads} species on the surface, whereas too high content of SO_4^{2-} caused agglomeration of TiO_2–SiO_2 particles to form many strong acid sites and too many O_{ads} species. The latter actually led to severe oxidation of NH_3 and obvious formation of stable sulfate salts to decrease consequently the $DeNO_x$ activity, selectivity and lifetime of the corresponding catalyst. Overall, the article demonstrated excellent $DeNO_x$ performances for a catalyst made using BFS because of its presence of proper amounts of $Al_2O_3/Fe_2O_3/SO_4^{2-}$ as the catalyst dopants or impurities from processing Ti-bearing BFS in making the catalyst. In fact, such dopants indeed obviously modified the support properties and chemical variability of active vanadium species, as was shown by the preceding results.

Acknowledgements

The authors are grateful to the financial support of Science and Technology Service Network Initiative of China (KFJ-SW-STS-

149), International Science and Technology Cooperation Program of China (2016YFE0128300) and postdoctoral fellowship of Japan Society for the Promotion of Science (JSPS by P15758).

References

1 W. Shan and H. Song, *Catal. Sci. Technol.*, 2015, **5**, 4280–4288.
2 Y. Zheng, A. D. Jensen and J. E. Johnsson, *Appl. Catal., B*, 2005, **60**, 253–264.
3 C. Wang, S. Yang, H. Chang, Y. Peng and J. Li, *Chem. Eng. J.*, 2013, **225**, 520–527.
4 R. Gao, D. Zhang, X. Liu, L. Shi, P. Maitarad, H. Li, J. Zhang and W. Cao, *Catal. Sci. Technol.*, 2013, **3**, 191–199.
5 Y. Pan, W. Zhao, Q. Zhong, W. Cai and H. Li, *J. Environ. Sci.*, 2013, **25**, 1703–1711.
6 M. Kobayashi, R. Kuma and A. Morita, *Catal. Lett.*, 2006, **112**, 37–44.
7 M. Kobayashi, R. Kuma, S. Masaki and N. Sugishima, *Appl. Catal., B*, 2005, **60**, 173–179.
8 W. Cha, S.-T. Yun and J. Jurng, *Phys. Chem. Chem. Phys.*, 2014, **16**, 17900–17907.
9 Z. Ma, X. Wu, Y. Feng, Z. Si, D. Weng and L. Shi, *Prog. Nat. Sci.*, 2015, **25**, 342–352.
10 L. Chen, J. Li and M. Ge, *J. Phys. Chem. C*, 2009, **113**, 21177–21184.
11 S. Yang, C. Wang, L. Ma, Y. Peng, Z. Qu, N. Yan, J. Chen, H. Chang and J. Li, *Catal. Sci. Technol.*, 2013, **3**, 161–168.
12 S. S. R. Putluru, L. Schill, A. Godiksen, R. Poreddy, S. Mossin, A. D. Jensen and R. Fehrmann, *Appl. Catal., B*, 2016, **183**, 282–290.
13 K. Cheng, J. Liu, Z. Zhao, Y. Wei, G. Jiang and A. Duan, *RSC Adv.*, 2015, **5**, 45172–45183.
14 W. Cha, S. Chin, E. Park, S.-T. Yun and J. Jurng, *Appl. Catal., B*, 2013, **140–141**, 708–715.
15 D.-s. Chen, L.-s. Zhao, T. Qi, G.-p. Hu, H.-x. Zhao, J. Li and L.-n. Wang, *Trans. Nonferrous Met. Soc. China*, 2013, **23**, 3076–3082.
16 L. Zhang, L. N. Zhang, M. Y. Wang, G. Q. Li and Z. T. Sui, *Miner. Eng.*, 2007, **20**, 684–693.
17 J. Yang, S. Lei, J. Yu and G. W. Xu, *J. Environ. Chem. Eng.*, 2014, **2**, 1007–1010.
18 K. Cheng, J. Liu, T. Zhang, J. Li, Z. Zhao, Y. Wei, G. Jiang and A. Duan, *J. Environ. Sci.*, 2014, **26**, 2106–2113.
19 Y. Peng, C. Liu, X. Zhang and J. Li, *Appl. Catal., B*, 2013, **140–141**, 276–282.
20 W. Zhao, Y. Tang, Y. Wan, L. Li, S. Yao, X. Li, J. Gu, Y. Li and J. Shi, *J. Hazard. Mater.*, 2014, **278**, 350–359.
21 H. K. Matralis, M. Ciardelli, M. Ruwet and P. Grange, *J. Catal.*, 1995, **157**, 368–379.
22 X. Zhao, L. Huang, S. Namuangruk, H. Hu, X. Hu, L. Shi and D. Zhang, *Catal. Sci. Technol.*, 2016, **6**, 5543–5553.
23 L. Yan, Y. Liu, H. Hu, H. Li, L. Shi and D. Zhang, *ChemCatChem*, 2016, **8**, 2267–2278.
24 T. Tran, J. Yu, L. Gan, F. Guo, D. Phan and G. Xu, *Catalysts*, 2016, **6**, 56.
25 X. Gao and I. E. Wachs, *Catal. Today*, 1999, **51**, 233–254.
26 H. S. Kibombo, R. Peng, S. Rasalingam and R. T. Koodali, *Catal. Sci. Technol.*, 2012, **2**, 1737–1766.
27 M. Casanova, K. Schermanz, J. Llorca and A. Trovarelli, *Catal. Today*, 2012, **184**, 227–236.
28 O. Ruzimuradov, S. Nurmanov, Y. Kodani, R. Takahashi and I. Yamada, *J. Sol-Gel Sci. Technol.*, 2012, **64**, 684–693.
29 W. Li and T. Zeng, *PLoS One*, 2011, **6**, e21082.
30 W. Zhao, Q. Zhong, T. Zhang and Y. Pan, *RSC Adv.*, 2012, **2**, 7906–7914.
31 Z. Li, Z. Wang and G. Li, *Powder Technol.*, 2016, **287**, 256–263.
32 F. Valighazvini, F. Rashchi and R. K. Nekouei, *Ind. Eng. Chem. Res.*, 2013, **52**, 1723–1730.
33 T. J. Pinnavaia, T. R. Pauly and S. S. Kim, in *Supported Catalysts and Their Applications*, ed. D. C. Sherrington and A. P. Kybett, The Royal Society of Chemistry, 2001, pp. 19–26, DOI: 10.1039/9781847551962-00019.
34 K. Sing, D. Everett, R. Haul, L. Moscou, R. Pierotti, J. Rouquerol and T. Siemieniewska, *Pure Appl. Chem.*, 1985, **57**, 603–619.
35 R. Jin, Z. Wu, Y. Liu, B. Jiang and H. Wang, *J. Hazard. Mater.*, 2009, **161**, 42–48.
36 A. Sorrentino, S. Rega, D. Sannino, A. Magliano, P. Ciambelli and E. Santacesaria, *Appl. Catal., A*, 2001, **209**, 45–57.
37 M. Kobayashi and M. Hagi, *Appl. Catal., B*, 2006, **63**, 104–113.
38 S. Liu, E. Guo and L. Yin, *J. Mater. Chem.*, 2012, **22**, 5031–5041.
39 J. P. Chen and R. T. Yang, *J. Catal.*, 1993, **139**, 277–288.
40 J. Y. Cho, W. H. Nam, Y. S. Lim, W.-S. Seo, H.-H. Park and J. Y. Lee, *RSC Adv.*, 2012, **2**, 2449–2453.
41 C. Marinescu, A. Sofronia, C. Rusti, R. Piticescu, V. Badilita, E. Vasile, R. Baies and S. Tanasescu, *J. Therm. Anal. Calorim.*, 2011, **103**, 49–57.
42 D. A. H. Hanaor and C. C. Sorrell, *J. Mater. Sci.*, 2011, **46**, 855–874.
43 R. Rejeb, L. Khalfallah Boudali, G. Delahay and C. Petitto, *Top. Catal.*, 2016, 1–8.
44 A. Rajaeiyan and M. M. Bagheri-Mohagheghi, *Adv. Manuf.*, 2013, **1**, 176–182.
45 C. Ren, W. Qiu and Y. Chen, *Sep. Purif. Technol.*, 2013, **107**, 264–272.
46 C. Orsenigo, L. Lietti, E. Tronconi, P. Forzatti and F. Bregani, *Ind. Eng. Chem. Res.*, 1998, **37**, 2350–2359.
47 R. Camposeco, S. Castillo and I. Mejía-Centeno, *Catal. Commun.*, 2015, **60**, 114–119.
48 L. Ma, J. Li, R. Ke and L. Fu, *J. Phys. Chem. C*, 2011, **115**, 7603–7612.
49 S. T. Choo, Y. G. Lee, I.-S. Nam, S.-W. Ham and J.-B. Lee, *Appl. Catal., A*, 2000, **200**, 177–188.
50 S. M. Jung and P. Grange, *Appl. Catal., B*, 2001, **32**, 123–131.
51 J. P. Chen and R. T. Yang, *J. Catal.*, 1990, **125**, 411–420.
52 F. Liu, Y. Yu and H. He, *Chem. Commun.*, 2014, **50**, 8445–8463.
53 L. Zhang, L. Shi, L. Huang, J. Zhang, R. Gao and D. Zhang, *ACS Catal.*, 2014, **4**, 1753–1763.
54 T. Mishra and K. M. Parida, *J. Colloid Interface Sci.*, 2006, **301**, 554–559.

55 M. Casanova, L. Nodari, A. Sagar, K. Schermanz and A. Trovarelli, *Appl. Catal., B*, 2015, **176–177**, 699–708.
56 H. Hu, S. Cai, H. Li, L. Huang, L. Shi and D. Zhang, *ACS Catal.*, 2015, **5**, 6069–6077.
57 Z. Fan, H. Guo, K. Fang and Y. Sun, *RSC Adv.*, 2015, **5**, 24795–24802.
58 S. Matsuda, T. Kamo, A. Kato, F. Nakajima, T. Kumura and H. Kuroda, *Ind. Eng. Chem. Prod. Res. Dev.*, 1982, **21**, 48–52.